

EUROPEAN ORGANISATION FOR NUCLEAR RESEARCH (CERN)



Submitted to: Phys. Rev. C

CERN-EP-2022-045
9th May 2022

Production of $\Upsilon(nS)$ mesons in Pb+Pb and pp collisions at 5.02 TeV

The ATLAS Collaboration

A measurement of the production of vector bottomonium states, $\Upsilon(1S)$, $\Upsilon(2S)$, and $\Upsilon(3S)$, in Pb+Pb and pp collisions at a center-of-mass energy per nucleon pair of 5.02 TeV is presented. The data correspond to integrated luminosities of 1.38 nb^{-1} of Pb+Pb data collected in 2018, 0.44 nb^{-1} of Pb+Pb data collected in 2015, and 0.26 fb^{-1} of pp data collected in 2017 by the ATLAS detector at the Large Hadron Collider. The measurements are performed in the dimuon decay channel for transverse momentum $p_T^{\mu\mu} < 30 \text{ GeV}$, absolute rapidity $|y^{\mu\mu}| < 1.5$, and Pb+Pb event centrality 0–80%. The production rates of the three bottomonium states in Pb+Pb collisions are compared with those in pp collisions to extract the nuclear modification factors as functions of event centrality, $p_T^{\mu\mu}$, and $|y^{\mu\mu}|$. In addition, the suppression of the excited states relative to the ground state is studied. The results are compared with theoretical model calculations.

1 Introduction

Quantum chromodynamics (QCD) predicts that at high temperatures and energy densities, hadronic matter undergoes a phase transition and turns into a state of deconfined quarks and gluons known as quark–gluon plasma (QGP). This state of matter is typically thought to be created in the collisions of two heavy nuclei at ultra-relativistic energies. In such collisions, heavy-flavor quarks, especially charm and bottom, are produced at an early stage in hard scattering processes and hence can probe QGP over its full evolution.

Formation of the QGP and the consequent modification to the heavy-quark potential is expected to lead to different quarkonium states dissolving at different temperatures of the medium [1]. This effect is known as sequential suppression [2]. While the excited states are dissociated just above the transition temperature $T_c \sim 155$ MeV needed to form the QGP, the ground states melt far above that value, creating a hierarchy in the measured suppression of quarkonium states. In particular, in Ref. [3], lattice calculations for the temperature-dependent behavior of the heavy-quark potential in full QCD theory were used to estimate the order of the suppression steps as functions of temperature and energy density. It was found that the $\Upsilon(1S)$ persists well above T_c , while $\Upsilon(2S)$ dissociates at about $1.1 T_c$ and $\Upsilon(3S)$ cannot exist at temperatures above T_c . Since then, quarkonium production and propagation through QGP have been extensively studied theoretically. Comprehensive reviews can be found in Refs. [4, 5].

Quarkonia dissociation in QGP can happen along with recombination of uncorrelated heavy quarks [6–8], which increases quarkonia yields. In this regard, it is interesting to compare bottomonium ($\Upsilon(1S)$, $\Upsilon(2S)$, $\Upsilon(3S)$, χ_b , etc.) to the charmonium family (J/ψ , $\psi(2S)$, χ_c , etc.), since recombination is expected to be much larger for the latter.

Experimentally, quarkonium suppression in nucleus–nucleus collisions has been studied extensively for both the bottomonia [9–12] and charmonia [13–19] families at RHIC and LHC energies. These measurements show strong suppression of quarkonia in nucleus–nucleus collisions compared to pp collisions, increasing for more central events, as well as stronger suppression of the excited Upsilon states ($\Upsilon(2S)$ and $\Upsilon(3S)$) relative to the ground state ($\Upsilon(1S)$).

In this paper, $\Upsilon(nS)$ production in pp and Pb+Pb collisions at $\sqrt{s} = 5.02$ TeV per nucleon–nucleon pair is studied as a function of transverse momentum ($p_T^{\mu\mu}$), rapidity, and Pb+Pb collision centrality.

2 The ATLAS detector

The ATLAS detector [20] at the LHC covers nearly the entire solid angle around the collision point.¹ It consists of an inner tracking detector surrounded by a thin superconducting solenoid, electromagnetic and hadronic calorimeters, and a muon spectrometer incorporating three large superconducting air-core toroidal magnets.

The inner-detector system (ID) is immersed in a 2 T axial magnetic field and provides charged-particle tracking in the range $|\eta| < 2.5$. The high-granularity silicon pixel detector covers the vertex region and typically provides four measurements per track, the first hit normally being in the insertable B-layer

¹ ATLAS uses a right-handed coordinate system with its origin at the nominal interaction point (IP) in the center of the detector and the z -axis along the beam pipe. The x -axis points from the IP to the center of the LHC ring, and the y -axis points upward. Cylindrical coordinates (r, ϕ) are used in the transverse plane, ϕ being the azimuthal angle around the z -axis. The pseudorapidity is defined in terms of the polar angle θ as $\eta = -\ln \tan(\theta/2)$, and the rapidity is defined as $y = (1/2)[(E + p_z)/(E - p_z)]$.

installed before Run 2 [21, 22]. It is followed by the silicon microstrip tracker, which usually provides eight measurements per track.

The muon spectrometer (MS) comprises separate trigger and high-precision tracking chambers measuring the deflection of muons in a magnetic field generated by the superconducting air-core toroids. The field integral of the toroids ranges between 2.0 and 6.0 T m across most of the detectors. A set of precision chambers covers the region $|\eta| < 2.7$ with three layers of monitored drift tubes, complemented by cathode strip chambers in the forward region, where the background is highest. Resistive plate chambers (RPCs) and thin gap chambers (TGCs) with a coarse position resolution but a fast response time are used primarily to trigger on muons in the ranges $|\eta| < 1.05$ and $1.05 < |\eta| < 2.4$ respectively.

The zero-degree calorimeters (ZDCs) are located symmetrically at $z = \pm 140$ m and cover $|\eta| > 8.3$. The ZDCs use tungsten plates as absorbers, and quartz rods sandwiched between the tungsten plates as the active medium. In Pb+Pb collisions, the ZDCs primarily measure “spectator” neutrons that do not interact hadronically when the incident nuclei collide.

Centrality in Pb+Pb collisions is determined by measuring the total transverse energy deposited in a liquid-argon forward calorimeter (FCal), which covers the pseudorapidity range $3.1 < |\eta| < 4.9$. The FCal is approximately 10 interaction lengths deep, and consists of three modules: the first, with copper absorbers, is optimized for electromagnetic measurements, while the other two, with tungsten absorbers, are mainly sensitive to energy depositions associated with produced hadrons.

A two-level trigger system is used to select events of interest [23]. The first-level (L1) trigger is implemented in hardware and uses a subset of detector information to reduce the event rate to a design value of at most 100 kHz. This is followed by the software-based high-level trigger (HLT), which reduces the event rate to about 1–4 kHz. The L1 muon trigger requires coincidences between hits on different RPC or TGC planes, which are used as a seed for the HLT algorithms. The HLT uses dedicated algorithms to incorporate information from both the MS and the ID, achieving position and momentum resolution close to that provided by the offline muon reconstruction, as shown in Ref. [23].

An extensive software suite [24] is used in the reconstruction and analysis of real and simulated data, in detector operations, and in the trigger and data acquisition systems of the experiment. The offline event selection required that events pass in-time pileup cuts based on the ZDCs energy.

3 Data selection and simulation samples

The results presented in this paper were obtained using pp data recorded in 2017 at a center-of-mass energy of 5.02 TeV as well as Pb+Pb data collected in 2015 and 2018 at 5.02 TeV per nucleon–nucleon pair.

The integrated luminosity of the analyzed pp collision samples is 0.26 fb^{-1} . The pp events were collected using a dimuon trigger which requires at least two spatially separated muon candidates at L1, while both satisfy the criterion of $p_T^\mu > 4 \text{ GeV}$ in the HLT. For the Pb+Pb analysis, the integrated luminosity is 0.44 nb^{-1} for the 2015 data sample and 1.38 nb^{-1} for the 2018 data sample. Pb+Pb events were collected using triggers which require at least one muon with $p_T^\mu > 4 \text{ GeV}$ at both L1 and the HLT, and at least one additional muon satisfying $p_T^\mu > 4 \text{ GeV}$ in the HLT, without requiring matching to L1.

Muon pairs were required to fulfill the following criteria: at least one reconstructed muon matching the HLT’s dimuon trigger, and both muons matching the HLT without an L1 trigger requirement; both muons satisfy the *Medium* identification criteria (described in Ref. [25]) without any requirements on TRT hits;

both muons are associated with the primary vertex reconstructed using all of the tracks in each event; the muon pair has a dimuon mass $7.7 < m_{\mu\mu} < 12.3$ GeV, dimuon transverse momentum $|p_T^{\mu\mu}| < 30$ GeV and dimuon rapidity $|y^{\mu\mu}| < 1.5$; the selected muon pair is re-fitted to a common vertex, with the vertex fit quality satisfying $\chi^2 < 100$ and the significance of the transverse displacement of the re-fitted vertex relative to the primary vertex satisfying $|L_{xy}/\sigma(L_{xy})| < 3$, where $\sigma(L_{xy})$ is the primary vertex resolution. The dimuon rapidity requirement was chosen to be $|y^{\mu\mu}| < 1.5$ because at more forward rapidities the Υ mass resolution starts to deteriorate quickly.

Monte Carlo (MC) simulation is used to study the $\Upsilon(nS)$ acceptance, the fit model used in Υ signal extraction, and the closure of muon reconstruction and identification corrections (due to residual biases associated with the yield correction procedure). The unpolarized prompt $\Upsilon(nS)$ in pp events were generated with the CTEQ6L1 [26] parton distribution function set in PYTHIA 8 [27] with subsequent decay in muon pairs. PYTHIA 8 implements prompt $\Upsilon(nS)$ production sub-processes using the non-relativistic QCD Color Octet mechanism [28]. Prompt $\Upsilon(nS)$ production includes prompt production from the hard interactions, as well as the radiative feed-down from $\chi_b \rightarrow \Upsilon(nS)\gamma$ decays. The production of nonprompt J/ψ , used for determining per-muon corrections, was simulated in PYTHIA 8 by forcing $b\bar{b}$ production and retaining only events consistent with J/ψ decays. The Pb+Pb MC sample was created by overlaying simulated PYTHIA 8 pp events with recorded minimum-bias Pb+Pb events, so that the “data overlay” simulation samples contain the same level of underlying-event activity as is present in the Pb+Pb data. The response of the ATLAS detector was simulated [29] using GEANT4 [30]. The MC events are reconstructed with the same algorithms as used in data.

4 Analysis procedure

4.1 Centrality definition in Pb+Pb

The transverse energy measured in the forward calorimeter, ΣE_T^{FCal} , in minimum bias events, is used to estimate the degree of overlap between the two colliding Pb nuclei. Each centrality class corresponds to a fixed percentile in the ΣE_T^{FCal} distribution of minimum-bias events using the procedure described in Ref. [31]. A Monte Carlo Glauber-based model [32] is used to calculate the mean number of participant nucleons, $\langle N_{\text{part}} \rangle$, and the mean nuclear overlap function, $\langle T_{\text{AA}} \rangle$, for each centrality class.

4.2 Corrections to raw invariant mass distributions

Before the dimuon invariant mass distributions are fit to extract Upsilon yields, each candidate dimuon pair is corrected with a weight that accounts for the $\Upsilon(nS)$ dimuon acceptance, trigger efficiency, and reconstruction efficiency.

The kinematic acceptance \mathcal{A} is defined as the probability that both muons from $\Upsilon \rightarrow \mu^+\mu^-$ decay pass the fiducial selection ($p_T^\mu > 4$ GeV and $|\eta^\mu| < 2.4$). The kinematic acceptance is calculated from a generator-level simulation separately for different $\Upsilon(nS)$ states as described in Ref. [33]. The acceptance correction also accounts for final-state radiation from one or both of the decay muons. In principle, the acceptance could depend on the spin-alignment of the $\Upsilon(nS)$. In this analysis, $\Upsilon(nS)$ mesons are assumed to be produced unpolarized, following the previous measurements in pp collisions [34–36]. These

measurements are consistent with no Υ polarization, but have large uncertainties. No extra systematic uncertainty due to Υ polarization is added in this study.

The dimuon reconstruction efficiency, $\varepsilon_{\text{reco}}(\mu_1\mu_2)$, is determined as the product of two single-muon reconstruction efficiencies. The single-muon reconstruction efficiency is factorized into ID track reconstruction efficiency and MS reconstruction efficiency. For pp collisions, the values of the reconstruction efficiency are obtained from the $J/\psi \rightarrow \mu^+\mu^-$ PYTHIA 8 simulation, and additional data-to-MC efficiency scale factors are derived using a $J/\psi \rightarrow \mu^+\mu^-$ tag-and-probe method [25] using pp data to account for residual differences between data and simulation. The same $J/\psi \rightarrow \mu^+\mu^-$ tag-and-probe method is employed to measure the muon reconstruction efficiency in Pb+Pb collisions. The ID reconstruction efficiency is obtained directly from Pb+Pb data, with a requirement on the transverse displacement of the J/ψ vertex to suppress potential biases from displaced muons. The MS reconstruction efficiency is obtained from the $J/\psi \rightarrow \mu^+\mu^-$ PYTHIA 8 simulation overlaid with minimum-bias Pb+Pb data, and additional data-to-MC scale factors are determined in Pb+Pb data to account for the small difference between data and simulation. The ID reconstruction efficiency is found to be larger than 99% in both pp and Pb+Pb collisions, with a weak centrality dependence at low p_T^μ in the latter case. The MS reconstruction efficiency at $p_T^\mu = 4$ GeV is about 65% in the barrel region ($|\eta_\mu| < 1.05$) and 75% in the endcap region ($1.05 < |\eta_\mu| < 2.4$), and the MS efficiency increases with p_T^μ and saturates at 95% around $p_T^\mu = 7$ GeV in both the barrel and endcap regions. Due to the absorption of most hadronic activity in the ATLAS calorimeters, the MS reconstruction efficiency has no centrality dependence. For a given muon pair, the dimuon trigger efficiency in pp collisions is factorized as the product of two single-muon efficiencies. The dimuon trigger efficiency in Pb+Pb collisions is the combined efficiency of either of the two muons matching HLT trigger while the other one matching HLT trigger without L1 trigger requirement.

The single-muon trigger efficiency is determined in data and simulation using a $J/\psi \rightarrow \mu^+\mu^-$ tag-and-probe method similar to that used for the muon reconstruction efficiency. Two different muon-trigger logic schemes are used in this analysis: 1) a full-chain muon trigger, which requires the formation of an L1 muon candidate that is subsequently confirmed in the HLT, and 2) a full-scan muon trigger, which is only performed in the HLT via a muon candidate search of the full MS system without any requirement at L1. The values of the full-chain muon trigger efficiency are determined from MC simulation, with data-to-MC scale factors determined from the pp data to take into account the difference between data and simulation. The same values are used for pp and Pb+Pb collisions, except that an additional centrality-dependent correction is applied to Pb+Pb data. The centrality-dependent correction is determined as the ratio of the trigger efficiency measured in Pb+Pb collisions as a function of centrality to the trigger efficiency in pp data. The full-chain muon trigger efficiency plateau value is found to be 70% in the barrel and 90% in the endcaps. The centrality-dependent correction factor is about 90% (100%) for the 0–10% (60–80%) centrality range. The full-scan muon trigger is only used in Pb+Pb collisions and its efficiency is determined directly from Pb+Pb data, using the tag-and-probe method. The full-scan trigger plateau is found to be 90% in both the barrel and endcap regions. The dimuon trigger efficiency in pp collisions is factorized as the product of two full-chain muon trigger efficiencies, and in Pb+Pb collisions the factorization form consisting of full-chain and full-scan muon trigger efficiencies, as detailed in Ref. [17], is used.

4.3 Upsilon signal extraction

Upsilon states are reconstructed in the $\mu^+\mu^-$ decay channel and their yields are determined via unbinned maximum-likelihood fits to the weighted dimuon invariant mass distributions, following the same procedure

for both pp and Pb+Pb data. Each of the three $\Upsilon(\text{nS})$ state signal shapes is described by a sum of Crystal Ball [37] and Gaussian functions.

The probability distribution function for the fit is defined as a normalized sum of three Υ signal components and a background component as

$$\text{pdf}(m_{\mu\mu}) = N_{\Upsilon(1S)} f_{\Upsilon(1S)}(m_{\mu\mu}) + N_{\Upsilon(2S)} f_{\Upsilon(2S)}(m_{\mu\mu}) + N_{\Upsilon(3S)} f_{\Upsilon(3S)}(m_{\mu\mu}) + N_{\text{bkg}} f_{\text{bkg}}(m_{\mu\mu}),$$

where $f_{\Upsilon(\text{nS})}(m_{\mu\mu}) = \omega F_G(m_{\mu\mu}; M_{\text{nS}}, \sigma_{\text{nS}}) + (1 - \omega) F_{\text{CB}}(m_{\mu\mu}; M_{\text{nS}}, 1.7\sigma_{\text{nS}}, \alpha, n)$; $N_{\Upsilon(\text{nS})}$ and N_{bkg} are the Upsilon and background yields, respectively; and F_G and F_{CB} are Gaussian and Crystal Ball functions, respectively, with ω representing relative weight of the Gaussian function. The quantities M_{nS} and σ_{nS} are the Gaussian function's mean and width for each Upsilon state, and α and n are F_{CB} tail parameters. The line shape parameters are assumed to be the same for all three Υ states since it is mostly determined by detector effects. The background shape, $f_{\text{bkg}}(m_{\mu\mu})$, is represented by a second-order polynomial at high $p_T^{\mu\mu}$ ($p_T^{\mu\mu} > 6$ GeV) and as a product of an error function and an exponential function at low $p_T^{\mu\mu}$.

The determination of the yield corrected for acceptance and efficiencies, $N_{\Upsilon(\text{nS})}^{\text{corr}}$, proceeds in several steps. First, a resonance-dependent weight, $w_{\text{total}}(\Upsilon(\text{nS}))$, is determined for each selected dimuon candidate as

$$w_{\text{total}}(\Upsilon(\text{nS})) = \frac{1}{\mathcal{A}(\Upsilon(\text{nS})) \cdot \varepsilon_{\text{reco}}(\mu_1\mu_2) \cdot \varepsilon_{\text{trig}}(\mu_1\mu_2) \cdot \varepsilon_{\text{pvAsso}}(\mu_1\mu_2)},$$

where $\mathcal{A}(\Upsilon(\text{nS}))$ is the acceptance for $\Upsilon(\text{nS}) \rightarrow \mu^+\mu^-$ decay, $\varepsilon_{\text{reco}}$ is the muon reconstruction efficiency, $\varepsilon_{\text{trig}}$ is the trigger efficiency, and $\varepsilon_{\text{pvAsso}}$ is the efficiency related to the primary-vertex association. Next, an unbinned maximum-likelihood fit to the weighted dimuon invariant mass distribution ($m_{\mu\mu}$) is performed to extract the $\Upsilon(\text{nS})$ yields. Three fits with an acceptance value corresponding to each state are performed to extract the yields for the three Υ states.

The mean and Gaussian width of the $\Upsilon(1S)$ signal, M_{1S} and σ_{1S} , are left unconstrained in each $p_T^{\mu\mu}$, $|y^{\mu\mu}|$ and centrality range, while the means and widths of $\Upsilon(2S)$ and $\Upsilon(3S)$ in the same range are fixed to $\Upsilon(1S)$ parameters scaled by the respective PDG [38] mass ratios. The widths of the CB functions are set by scaling the corresponding Gaussian widths by a constant factor, 1.7, which was determined in a previous analysis [39] and validated with MC studies. The relative weight of the Gaussian and CB functions, ω , is not constrained, and has the same value for all three Upsilon states. For the pp collision analysis, the CB function parameter α , which defines the point at which the low-mass tail transitions from a Gaussian shape to a power-law shape, was fixed to the value obtained from $\Upsilon(1S)$ MC samples, while n , which describes the shape of the tail, was a free parameter. For Pb+Pb collisions, both α and n were fixed to the values from the fit for pp collisions, for each kinematic selection. The nominal signal fit model described above was validated by fitting the signal MC samples in various $p_T^{\mu\mu}$, $|y^{\mu\mu}|$ and centrality intervals.

The background functional form varies with dimuon $p_T^{\mu\mu}$. For $p_T^{\mu\mu} > 6$ GeV the background is parameterized as a second-order polynomial. However, for lower $p_T^{\mu\mu}$ ($p_T^{\mu\mu} < 6$ GeV), and for the integrated over $p_T^{\mu\mu}$ fits, in order to describe the turn-on behavior of the dimuon acceptance caused by the single-muon transverse momentum requirement, an error function multiplied by an exponential function is used. The background model parameters are initialized using a background-enriched sample, which consists of events with same-sign muon pairs, as well as a control sample consisting primarily of muons from b-hadron decays. The control sample is produced by requiring at least one of the two muons to satisfy $|d_0|/\sigma_{d_0} > 2$ or $|z_0 \sin(\theta)| > 0.2$ mm, where d_0 and z_0 are the distances of closest approach of the muon to the primary vertex in the plane perpendicular to the beam and in the beam direction, respectively. After using the

background distributions to determine the relevant parametrizations, the full model including signal and background contributions is used to fit the data, with the slope of the exponential function allowed to float.

Figure 1 shows an example of the fit to the dimuon mass plots for pp (left) and 0–80% centrality $Pb+Pb$ (right) collisions for the inclusive $p_T^{\mu\mu}$ and $|y^{\mu\mu}|$ selection. The lower panels show the pull distribution, which represents the distance between data points and fit function normalized by the data points statistical uncertainty: $(Data - Fit)/\sigma(Data)$. The goodness of the fit is assessed by calculating the reduced chisquare, χ^2/NDF , summing the squared deviations of the data points from the fit (weighted by the inverse errors) and then dividing by the number of degrees of freedom (NDF) in the fit. Typically, χ^2/NDF for the fits varies from ~ 2.5 to ~ 1 for pp and from ~ 2 to ~ 1 for $Pb+Pb$, indicating that the data and model agree within statistical uncertainties. The extracted values of χ^2/NDF decrease with $p_T^{\mu\mu}$, indicating that the fit quality improves with $p_T^{\mu\mu}$. Some relatively large χ^2/NDF values are also found and can be explained by deviations of the functions used for background description from the actual background at the edges of the fit range.

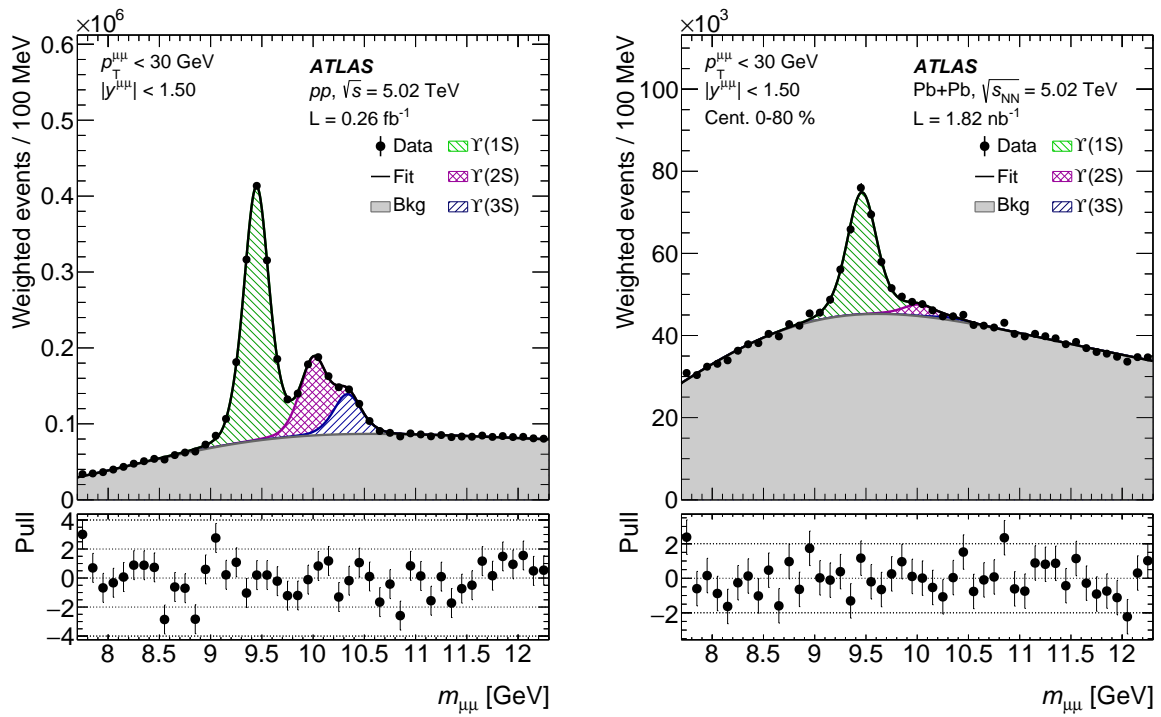


Figure 1: Dimuon invariant mass distributions with the fit results for pp (left) and $Pb+Pb$ (right) collisions at 5.02 TeV. The various curves are explained in the legend. Pull distributions are shown in the lower panels. For this selection, χ^2/NDF is 2.7 for pp and 1.3 for $Pb+Pb$.

4.4 Systematic uncertainties

The main sources of point-by-point uncorrelated systematic uncertainties pertain to the corrections for muon reconstruction and trigger efficiencies, and the yield extraction. For the lowest $p_T^{\mu\mu}$ range, the final-state radiation correction is also a significant contribution. Other, subdominant sources of systematic

uncertainty considered in this study are the primary-vertex association uncertainty and bin migration due to momentum resolution. Finally, the Upsilon states are assumed to be unpolarized and no extra systematic uncertainty is assigned to cover this assumption.

The systematic uncertainty in the MS reconstruction efficiency is dominated by the uncertainty in the data-to-MC scale-factor determination. The scale-factor uncertainty is evaluated following Ref. [25] by changing the tag-muon selection criteria and varying the line-shapes in the efficiency extraction fit procedure in the data. The uncertainty related to the ID reconstruction efficiency, which is close to 1, is estimated by comparing the results while varying this efficiency in both up and down directions by one standard deviation.

The systematic uncertainty in the muon trigger efficiency is also dominated by the tag-and-probe efficiency determination procedure. For Pb+Pb collisions, an additional systematic uncertainty associated with the centrality-dependent correction is included. This uncertainty is evaluated by comparing the centrality-dependence-corrected Pb+Pb efficiency with the pp efficiency as a function of p_T^μ . Individual variations described above are added in quadrature to form the total systematic uncertainty of the efficiency corrections.

The sensitivity of the signal extraction to the choice of a particular fit model is evaluated by varying the line-shape of each fit component. The maximum variation between the recalculated values and the central value is used to estimate their uncertainty. Eight variations are considered, and these can be categorized into three groups: signal resolution (width of the peak), shape of the final-state radiation tail, and background shape. The final uncertainty from the fit model is obtained by calculating the difference between the maximum and the minimum yield from the eight line-shape variations and dividing by $\sqrt{12}$, assuming a flat distribution.

The uncertainty in the Υ acceptance due to the final-state radiation correction was calculated by comparing the result of a fully simulated acceptance calculation with that obtained using an MC sample designed for a high-precision determination of the acceptance. The signal Monte Carlo samples were processed with a fast simulation [29] which relies on a parameterization of the calorimeter response [40]. This uncertainty is only important for the lowest $p_T^{\mu\mu}$ range.

The global uncertainty of the integrated luminosity for the 2017 pp data is 1.6%, derived using methods described in Ref. [41]. Primary vertex association uncertainty, which results mostly from small discrepancies between data and MC, was studied by varying the primary vertex association requirements. Since the primary-vertex association affects all Upsilon state yields in the same way, it is treated as a global uncertainty together with those of the pp luminosity and T_{AA} . The combined systematic uncertainty for the luminosity and primary-vertex association in pp data is 2.6%. For Pb+Pb collisions, the global systematic uncertainty of $\langle T_{AA} \rangle$ is estimated by varying the Glauber model parameters as detailed in Ref. [31]. The combined systematic uncertainty for $\langle T_{AA} \rangle$ and primary-vertex association in Pb+Pb collisions is 3.7%.

Systematic uncertainties in pp and Pb+Pb collisions are summarized in Table 1. While some systematic uncertainties for R_{AA} values and excited-state to ground-state double ratios are correlated (e.g. the acceptance) and cancel out in the ratios, most of the systematic uncertainties are not completely correlated and are estimated by directly studying their effects on the ratios.

Table 1: Summary of the sources of systematic uncertainty.

Collision type	Sources	$\Upsilon(1S)$ [%]	$\Upsilon(nS)$ [%]	$\Upsilon(nS)/\Upsilon(1S)$ [%]
<i>pp</i> collisions	Luminosity	1.6	1.6	-
	Acceptance	0.3–9.3	0.2–4.1	-
	Efficiency	2.7–7.0	2.8–4.0	3.0–7.1
	Signal extraction	3.1–10.2	4.3–11.9	4.5–12.2
	Bin migration	<1	<1	-
	Primary-vertex association	2.0	2.0	-
<i>Pb+Pb</i> collisions	$\langle T_{AA} \rangle$	0.8–8.2	0.8–8.2	-
	Acceptance	0.3–9.3	0.2–4.1	-
	Efficiency	4.0–15.0	3.9–25.3	4.4–28.8
	Signal extraction	3.8–16.3	14.6–28.7	16.6–31.5
	Bin migration	<2	<2	-
	Primary-vertex association	3.4	3.4	-

5 Results

5.1 Differential cross-section

Differential $\Upsilon(nS)$ production cross-sections in *pp* collisions are measured according to the relation

$$\frac{d^2\sigma_{\Upsilon(nS)}}{dp_T^{\mu\mu} dy^{\mu\mu}} \times \mathcal{B}(\Upsilon(nS) \rightarrow \mu^+ \mu^-) = \frac{N_{\Upsilon(nS)}^{\text{corr}}}{\Delta p_T^{\mu\mu} \times \Delta y^{\mu\mu} \times \int \mathcal{L} dt},$$

where $\mathcal{B}(\Upsilon(nS) \rightarrow \mu^+ \mu^-)$ is the dimuon decay branching fraction, $N_{\Upsilon(nS)}^{\text{corr}}$ is the $\Upsilon(nS)$ yield corrected for acceptance and efficiencies, $\Delta p_T^{\mu\mu}$ and $\Delta y^{\mu\mu}$ are the bin widths in $p_T^{\mu\mu}$ and $y^{\mu\mu}$, and $\int \mathcal{L} dt$ is the integrated luminosity.

The $\Upsilon(nS)$ differential cross-sections in *pp* collisions at 5.02 TeV, multiplied by the respective dimuon branching fractions, are shown as a function of $p_T^{\mu\mu}$ in the left panel of Figure 2.

The per-event yields of $\Upsilon(nS)$ states in *Pb+Pb* collisions are defined by

$$N_{\text{AA}} = \frac{N_{\Upsilon(nS)}^{\text{corr}}}{\Delta p_T^{\mu\mu} \times \Delta y^{\mu\mu} \times N_{\text{evt}}},$$

where N_{evt} is the total number of minimum-bias *Pb+Pb* collisions in each centrality class. In particular, this number is 1.02×10^9 for the 0–10% centrality interval. Per-event Upsilon yields in *Pb+Pb* collisions divided by $\langle T_{AA} \rangle$ are shown in the right panel of Figure 2. The results for $\Upsilon(3S)$ mesons are not shown because their peaks are not statistically significant in *Pb+Pb* collisions.

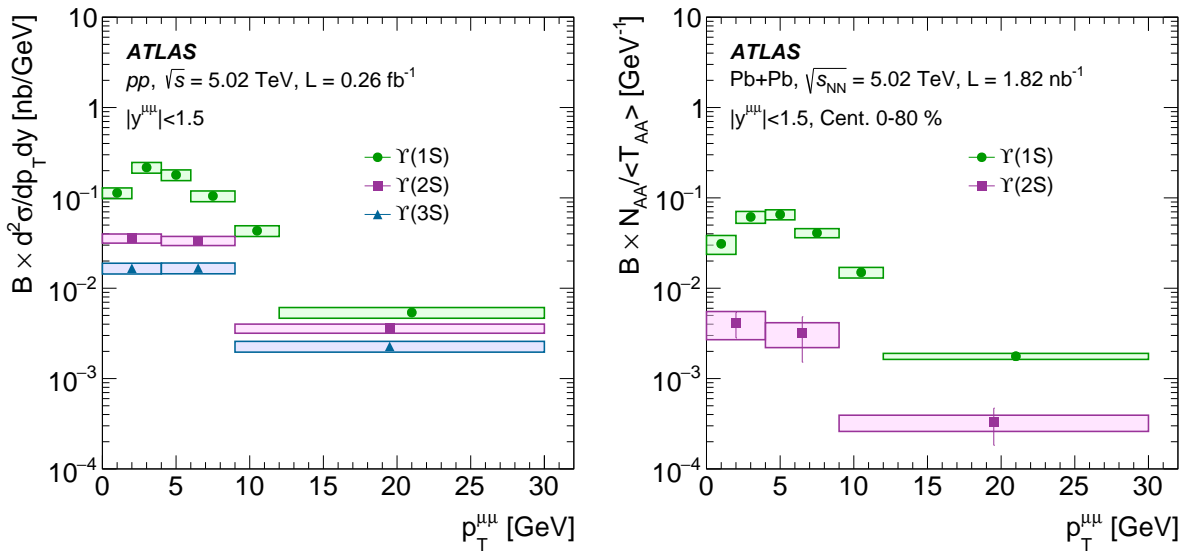


Figure 2: Production cross-sections of $\Upsilon(1S)$, $\Upsilon(2S)$, and $\Upsilon(3S)$ mesons as a function of $p_T^{\mu\mu}$ in pp collisions (left) and per-event yields in $Pb+Pb$ collisions (right) at 5.02 TeV. Error bars indicate the statistical uncertainties and boxes represent the systematic uncertainties. Not shown are the correlated systematic uncertainties of 2.6% for luminosity and primary-vertex association in pp and 3.7% for $\langle T_{AA} \rangle$ and primary-vertex association in $Pb+Pb$ collisions.

5.2 Nuclear modification factor

The modifications of bottomonium production yields in $Pb+Pb$ collisions relative to the pp system are quantified by the nuclear modification factor R_{AA} , which can be defined for each centrality interval as

$$R_{AA} = \frac{N_{AA}}{\langle T_{AA} \rangle \times \sigma^{pp}},$$

where N_{AA} is the observed per-event yield of bottomonium states in $Pb+Pb$ collisions, and σ^{pp} is the bottomonium production cross-section in pp collisions at the same collision energy.

Figure 3 shows the R_{AA} values of $\Upsilon(nS)$ as functions of $\langle N_{part} \rangle$ (top), dimuon $p_T^{\mu\mu}$ (bottom left), and $|y^{\mu\mu}|$ (bottom right). The centrality-integrated results are also shown in the right panel of the top plot. In addition to the results for $\Upsilon(1S)$ and $\Upsilon(2S)$, only the combined result for the two excited states, $\Upsilon(2S+3S)$, is presented because the $\Upsilon(3S)$ peak is not statistically significant in the $Pb+Pb$ data. The $\Upsilon(nS)$ states are observed to be suppressed over the whole kinematic range investigated, and the R_{AA} values of $\Upsilon(2S)$ and $\Upsilon(2S+3S)$ are always lower than those of $\Upsilon(1S)$. The R_{AA} value decreases with $\langle N_{part} \rangle$ for all three states. No strong $p_T^{\mu\mu}$ or $|y^{\mu\mu}|$ dependence is observed. When no statistically significant non-zero yield was extracted for a particular kinematic selection, 95% confidence level upper limit was calculated.

5.3 Excited-state to ground-state double ratios

The suppression of different Upsilon states can be compared by constructing an excited-state to ground-state double ratio of nuclear modification factors. The advantage of measuring the double ratios is that the

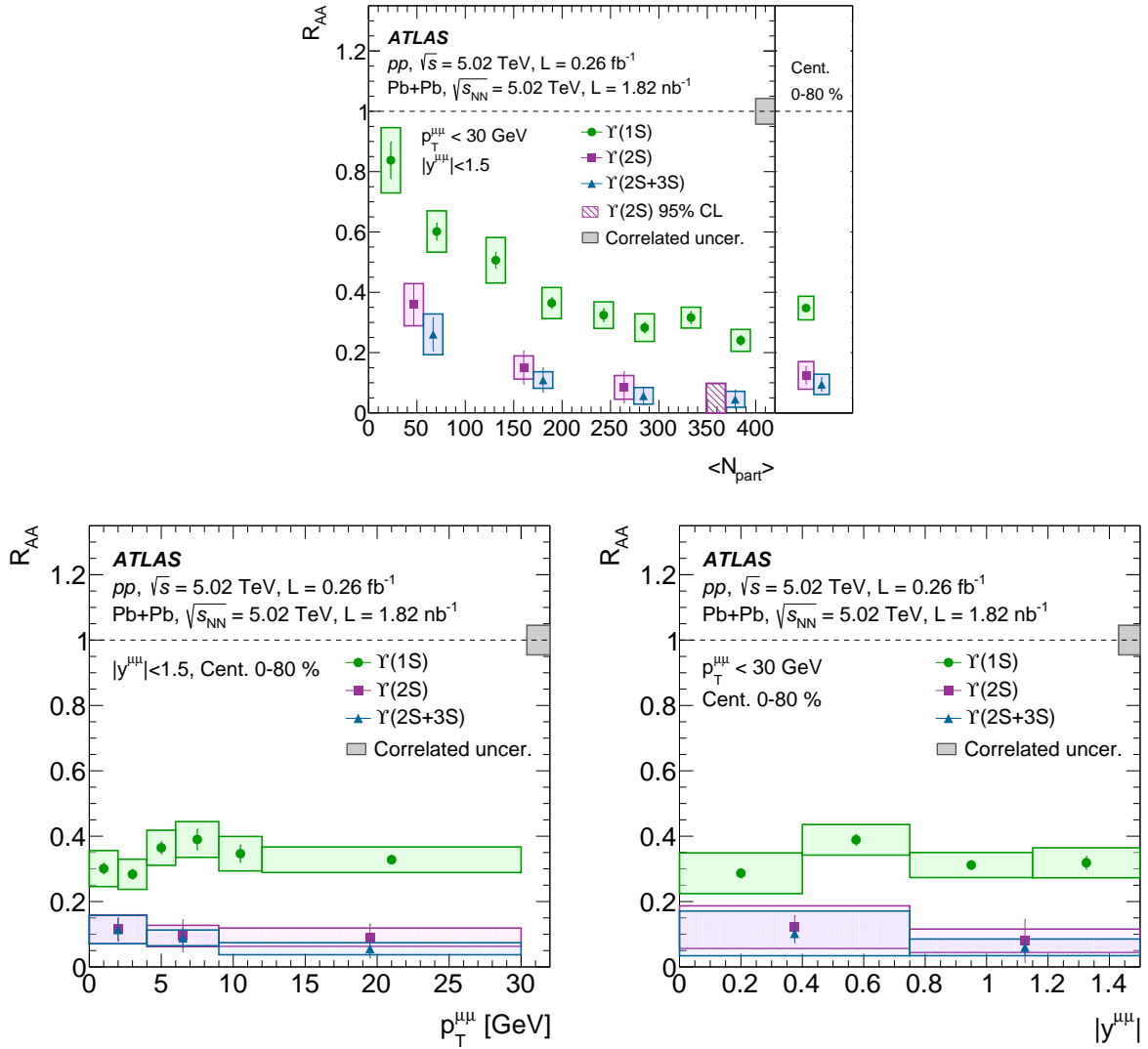


Figure 3: The nuclear modification factor R_{AA} of $\Upsilon(1S)$, $\Upsilon(2S)$, and $\Upsilon(2S+3S)$ as functions of centrality (top), $p_T^{\mu\mu}$ (bottom left), and $|y^{\mu\mu}|$ (bottom right) at 5.02 TeV. Error bars indicate the statistical uncertainties and boxes represent the systematic uncertainties. The gray boxes around $R_{AA} = 1$ correspond to the global systematic uncertainty. The right panel of the top plot shows the R_{AA} results integrated over centrality.

acceptance and efficiency corrections partially cancel out, and the overall systematic uncertainty is reduced. Although defined in terms of the individual nuclear suppression factors, the double ratio can be understood as being defined as the ratio of the yields of excited states $\Upsilon(2S)$, $\Upsilon(3S)$ or of combined yield of the two excited states ($\Upsilon(2S + 3S)$) to the yield of the ground state $\Upsilon(1S)$ in $Pb+Pb$ collisions, divided by the same ratio in pp collisions.

$$\rho_{AA}^{\Upsilon(nS)/\Upsilon(1S)} = R_{AA}(\Upsilon(nS))/R_{AA}(\Upsilon(1S)).$$

Figure 4 shows the $\rho_{AA}^{\Upsilon(nS)/\Upsilon(1S)}$ for $\Upsilon(2S)$ and $\Upsilon(2S+3S)$ as functions of N_{part} (top), $p_T^{\mu\mu}$ (bottom left), and $|y^{\mu\mu}|$ (bottom right). The centrality-integrated results are also shown in the right panel of the top plot.

The $\rho_{AA}^{\gamma(nS)/\gamma(1S)}$ values for $\gamma(2S)$ and $\gamma(2S+3S)$ are always less than one, indicating the excited states are more suppressed than the ground state. The centrality-dependent $\rho_{AA}^{\gamma(nS)/\gamma(1S)}$ shows a slightly decreasing trend toward more central collisions, but no $p_T^{\mu\mu}$ or $|y^{\mu\mu}|$ dependence is observed.

These results are consistent with previous measurements of Upsilon suppression at LHC energies by the CMS [11] and ALICE [12] experiments.

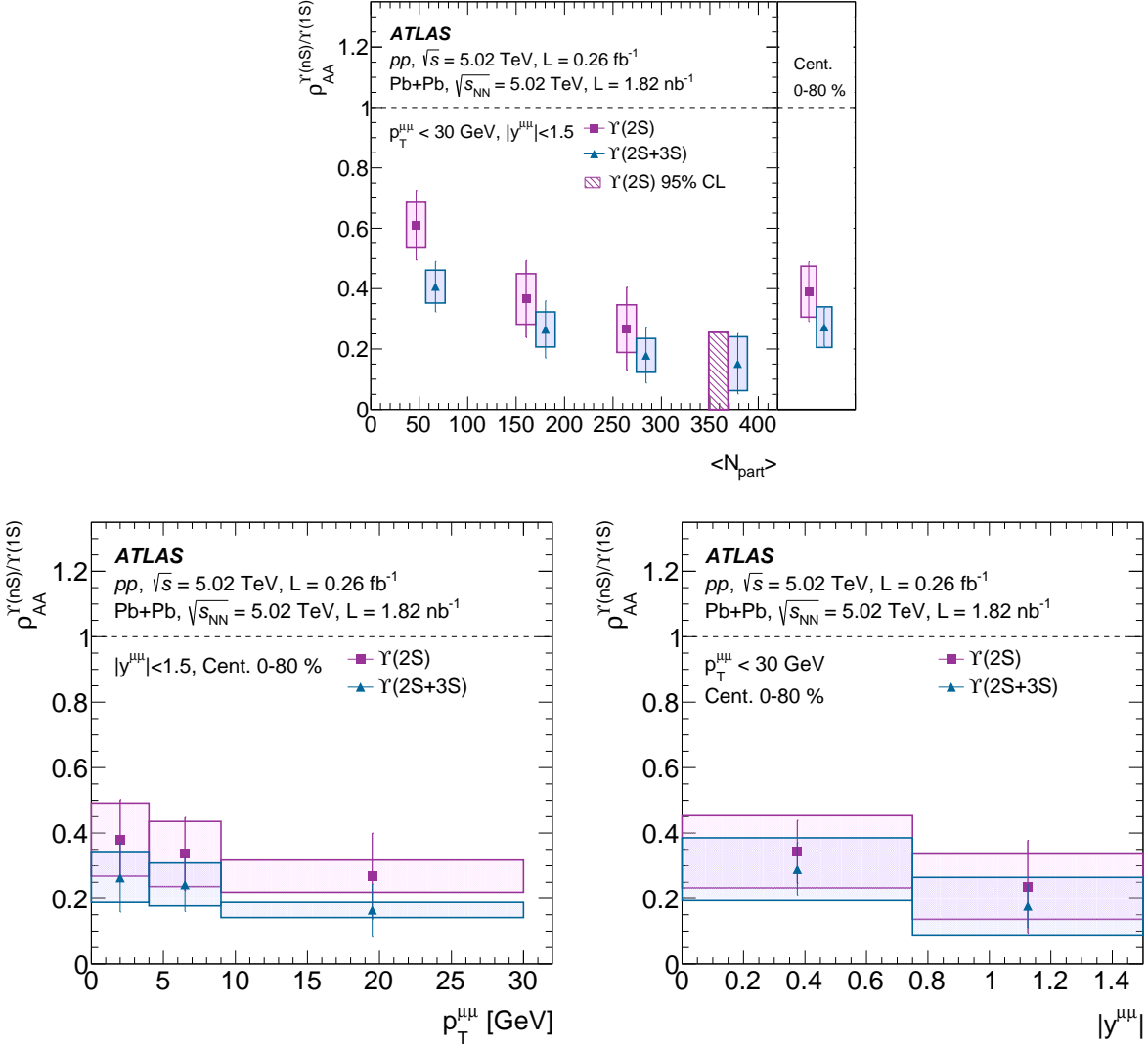


Figure 4: The double ratio $\rho_{AA}^{\gamma(nS)/\gamma(1S)}$ for $\gamma(2S)$ and $\gamma(2S+3S)$ as functions of centrality (top), $p_T^{\mu\mu}$ (bottom left), and $|y^{\mu\mu}|$ (bottom right) at 5.02 TeV per nucleon–nucleon pair. Error bars indicate the statistical uncertainties and boxes represent the systematic uncertainties. The right panel of the top plot shows the results integrated over centrality.

5.4 Theory comparisons

Figure 5 shows the R_{AA} of $\Upsilon(1S)$ and $\Upsilon(2S)$ and the double ratio $\rho_{AA}^{\Upsilon(2S)/\Upsilon(1S)}$ compared with a calculation by N. Brambilla et al. in Ref. [42]. This model uses potential NRQCD and the formalism of open quantum systems to numerically solve the Lindblad equation using a stochastic unraveling called the quantum trajectories algorithm. Heavy-quark interactions with the strongly coupled medium are encoded in the two nonperturbative transport coefficients: the heavy-quark momentum diffusion coefficient and its dispersive counterpart. The authors of Ref. [42] have run variations of these parameters within reasonable ranges.

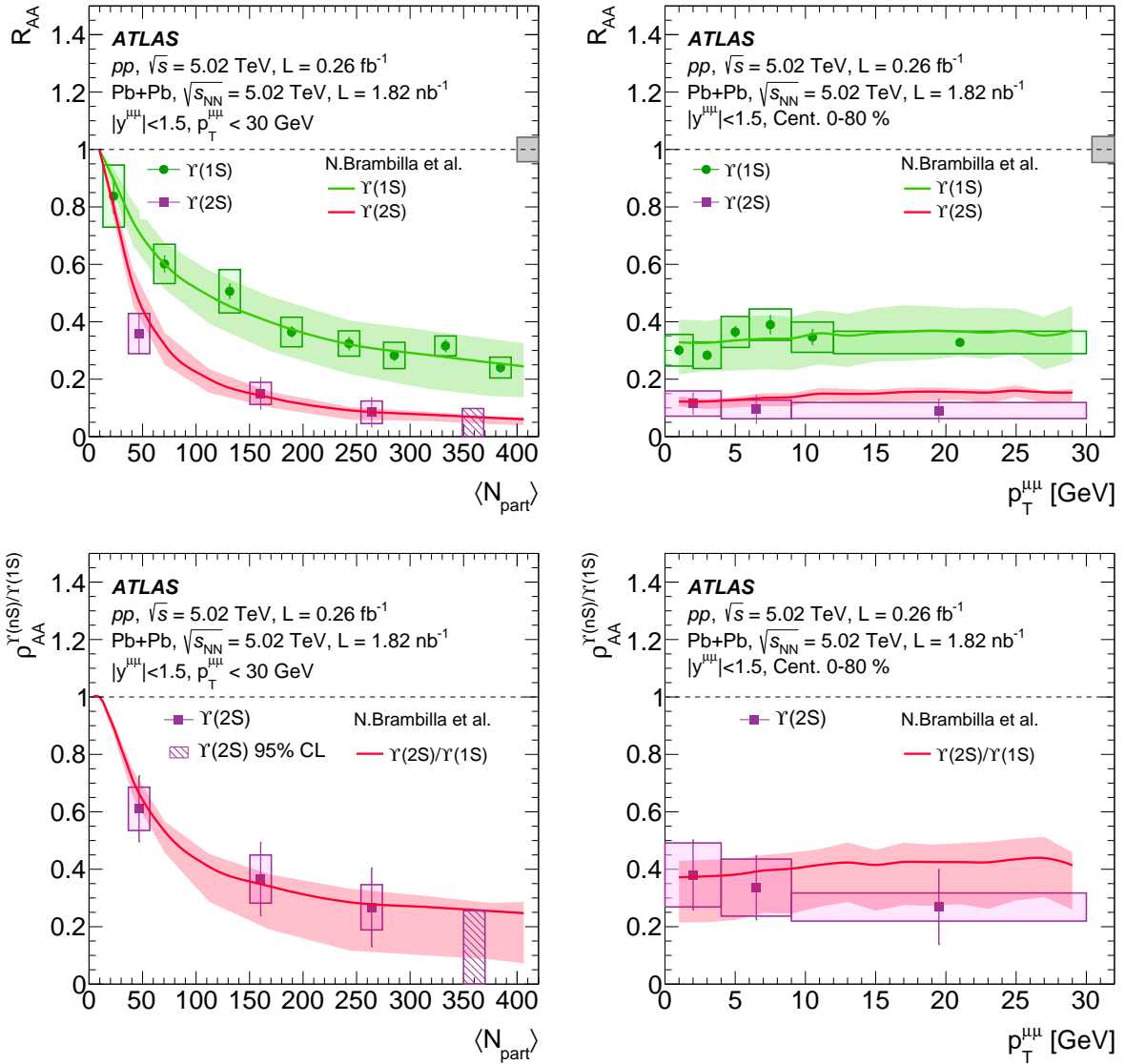


Figure 5: The nuclear modification factor R_{AA} of $\Upsilon(1S)$ and $\Upsilon(2S)$ (top row) and the double ratio $\rho_{AA}^{\Upsilon(nS)/\Upsilon(1S)}$ for $\Upsilon(1S)$ and $\Upsilon(2S)$ (bottom row) as functions of centrality (left column) and $p_T^{\mu\mu}$ (right column) at 5.02 TeV per nucleon–nucleon pair compared to a calculation by N. Brambilla et al., Ref. [42] (solid curves). Color bands represent model uncertainties due to variation of the model parameters.

Figure 6 shows the R_{AA} of $\Upsilon(1S)$, $\Upsilon(2S)$ and $\Upsilon(2S+3S)$, and the double ratio $\rho_{AA}^{\Upsilon(nS)/\Upsilon(1S)}$ for $\Upsilon(2S)$ and $\Upsilon(2S+3S)$ compared to a calculation by X. Du et al. in Ref. [43]. This model uses a kinetic-rate equation approach including regeneration and has four dimensionless parameters which characterize the temperature dependence of the pertinent screening masses. These parameters are extracted through the fits to the data already available at RHIC and LHC. The band corresponding to the 95% confidence interval is shown in the figure.

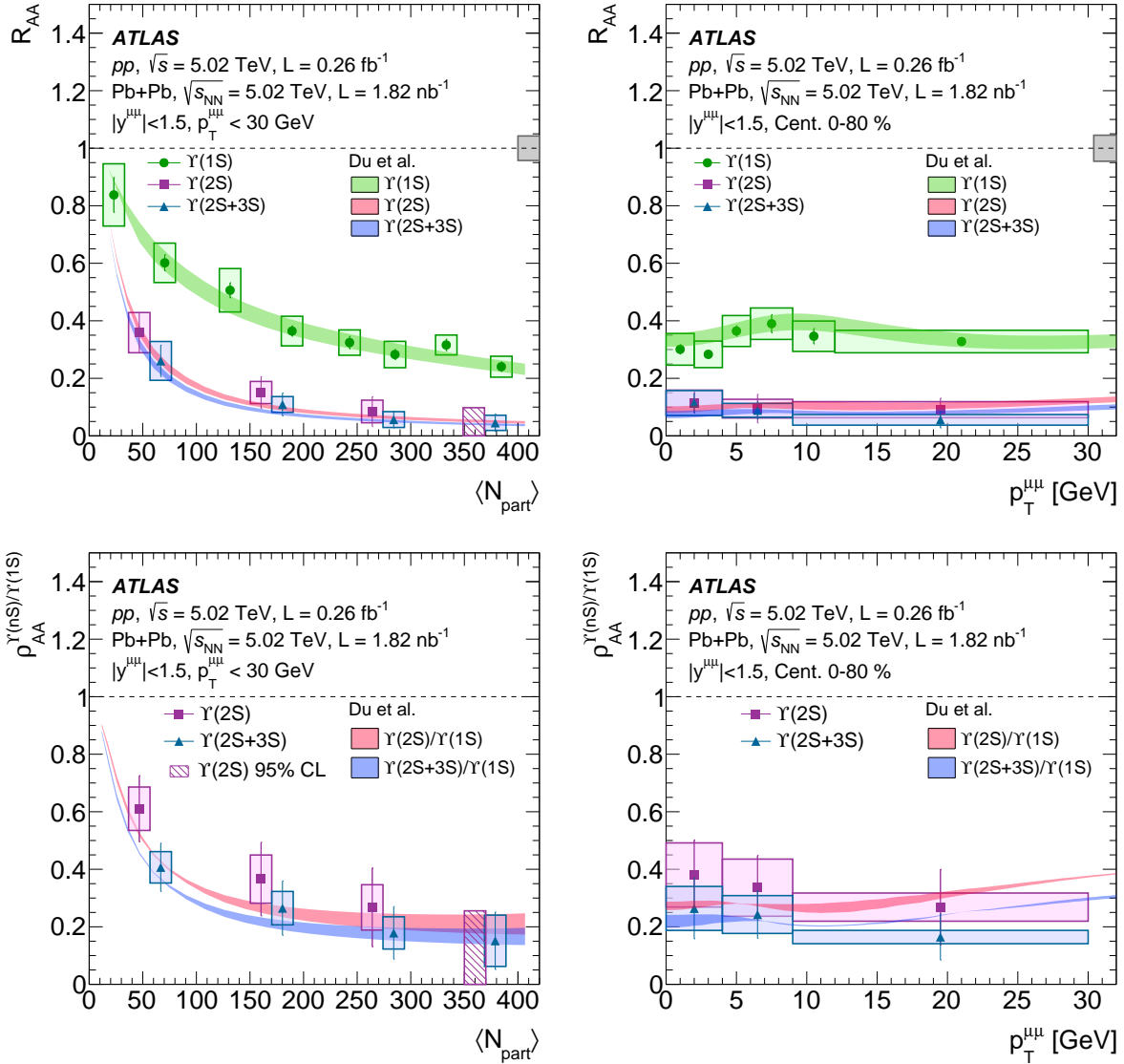


Figure 6: The nuclear modification factor R_{AA} of $\Upsilon(1S)$ and $\Upsilon(2S)$ (top row) and the double ratio $\rho_{AA}^{\Upsilon(nS)/\Upsilon(1S)}$ for $\Upsilon(2S)$ (bottom row) as functions of centrality (left) and $p_T^{\mu\mu}$ (right) at 5.02 TeV per nucleon–nucleon pair compared to a calculation by X. Du et al., Ref. [43]. The bands represent 95% confidence level (CL) limits.

Figure 7 shows the R_{AA} of $\Upsilon(1S)$, $\Upsilon(2S)$ and $\Upsilon(2S+3S)$, as well as the double ratio $\rho_{AA}^{\Upsilon(nS)/\Upsilon(1S)}$ for $\Upsilon(1S)$ and $\Upsilon(2S)$, compared to a calculation by X. Yao et al. in Ref. [8]. This model uses a framework with coupled transport equations for open heavy-flavor and quarkonium states in order to describe their transport

inside the quark–gluon plasma, including regeneration. Cold nuclear matter effects are included by using nuclear parton distribution functions for the initial primordial heavy-flavor production. A calibrated $(2 + 1)$ -dimensional viscous hydrodynamic model is used to describe the bulk QCD medium. The model depends on the choice of nucleus parton distribution function (nPDF) and two coupling constant parameters, α_s and α_s^{pot} , which are varied by $\pm 10\%$ from their nominal values.

All three models are in agreement with the data within experimental and theoretical uncertainties. It is notable that all three theoretical results were calculated after the publication of a CMS measurement of Υ suppression in Ref. [11] at the same beam energy.

Reference [44] quotes dissociation temperatures in the case of an isotropic QGP of < 192 MeV, 228 MeV, and 593 MeV for the $\Upsilon(3S)$, $\Upsilon(2S)$, $\Upsilon(1S)$ states, respectively. It is notable that the $\Upsilon(1S)$ has a substantial decay feed-down fraction from $\Upsilon(2S)$, $\Upsilon(3S)$, and $\chi_b(1S)$, $\chi_b(2S)$ states, and that only about half of $\Upsilon(1S)$ are directly produced. Thus, the suppression at the level of approximately 0.25 – 0.30 for the $\Upsilon(1S)$ observed in central Pb+Pb collisions indicates at least some suppression of the directly produced $\Upsilon(1S)$, which has important implications regarding the temperatures achieved in the QGP.

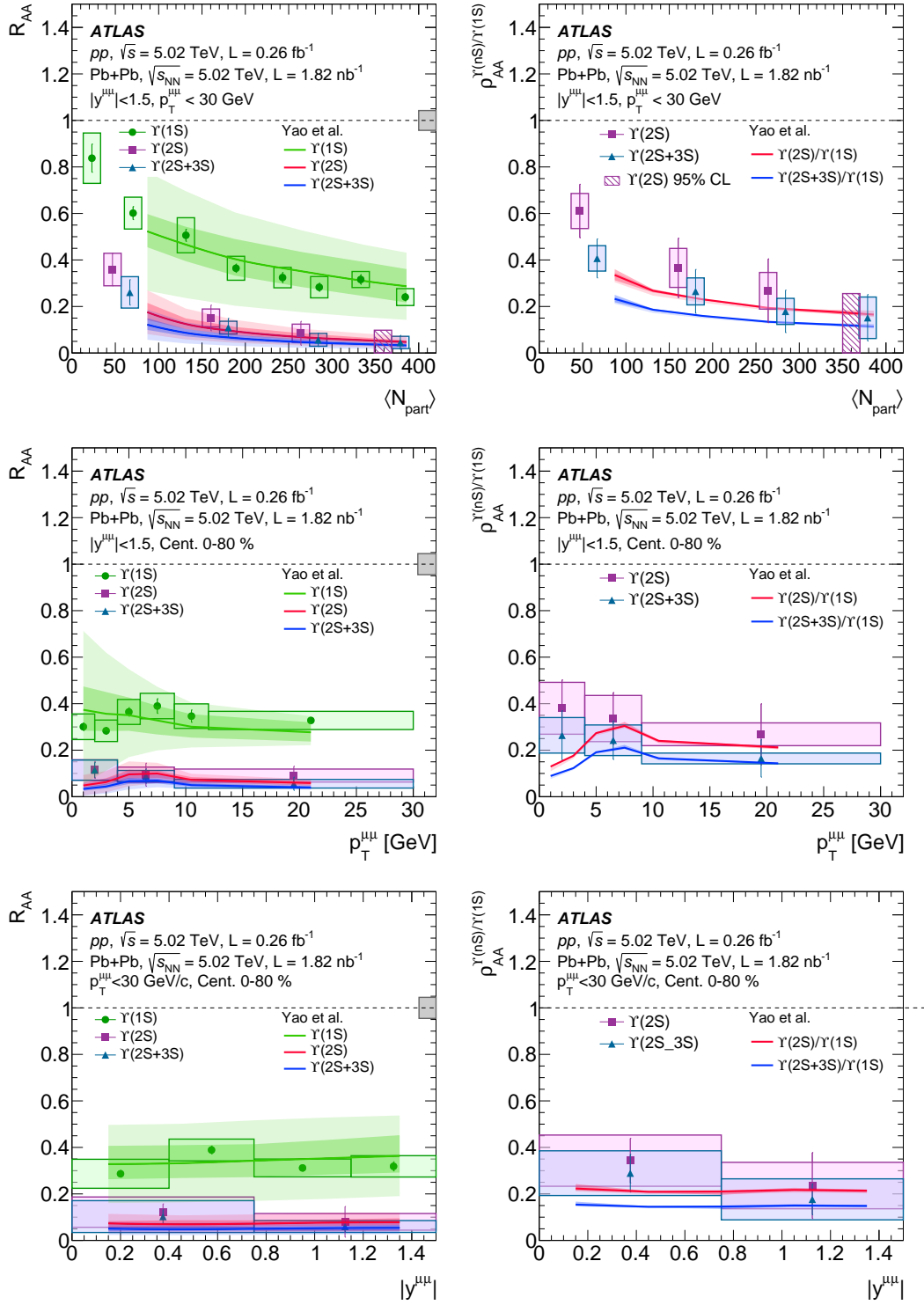


Figure 7: The nuclear modification factor R_{AA} of $\gamma(1S)$, $\gamma(2S)$ and $\gamma(2S+3S)$ (left column) and the double ratio $\rho_{AA}^{\gamma(nS)/\gamma(1S)}$ for $\gamma(2S)$ and $\gamma(2S+3S)$ (right column) as functions of centrality (top row), $p_T^{\mu\mu}$ (center row) and rapidity (bottom row) at 5.02 TeV per nucleon–nucleon pair compared to a calculation by X. Yao et al., Ref. [8] (solid curves). Dark color bands show theory uncertainty due to the nPDF choice. Light color bands show model uncertainties due to varying the calculation parameters by $\pm 10\%$.

6 Conclusions

This paper presents a measurement of $\Upsilon(nS)$ yields in pp and Pb+Pb data at 5.02 TeV per nucleon–nucleon collision. The measurement uses data from pp collisions collected in 2017 with a total integrated luminosity of 0.26 fb^{-1} and Pb+Pb collisions collected in 2015 and 2018 with total integrated luminosities of 0.44 nb^{-1} and 1.38 nb^{-1} respectively, recorded by the ATLAS experiment at the LHC. The pp and Pb+Pb measurements are used to obtain the nuclear modification factor for $\Upsilon(1S)$, $\Upsilon(2S)$, and $\Upsilon(2S+3S)$, as well as excited-state to ground-state double ratios of R_{AA} for $\Upsilon(2S)$ and $\Upsilon(2S+3S)$ as functions of transverse momentum, rapidity, and centrality. Both the $\Upsilon(1S)$ and $\Upsilon(2S)$ yields are suppressed with increasing centrality in Pb+Pb compared to those in pp collisions, and the excited states are shown to be stronger suppressed than the ground state, resulting in double ratios smaller than one. The R_{AA} value for $\Upsilon(2S+3S)$ appears to be systematically lower than that for $\Upsilon(2S)$, and so are the corresponding double ratios, which indicates that the $\Upsilon(3S)$ state is suppressed more than $\Upsilon(2S)$.

Suppression of the $\Upsilon(1S)$ observed at the level of about 0.25–0.30 in central Pb+Pb collisions indicates at least some suppression of the directly produced $\Upsilon(1S)$, given the sizable decay feed-down fraction from higher states, and this has important implications regarding the temperatures achieved in the QGP.

The measured nuclear modification factors and double ratios are found to be consistent with the previous CMS measurement [45]. The previous measurement by ALICE [12] were at a lower \sqrt{s} and at very forward rapidities, which makes direct comparison difficult. All theoretical calculations considered in this paper describe the data well and incorporate deconfinement as a key ingredient in the suppression of the Upsilon yields. Further discrimination between the different implementations of these deconfinement effects require additional precision data from upcoming runs at RHIC and the LHC.

References

- [1] T. Matsui and H. Satz, *J/ψ suppression by quark-gluon plasma formation*, *Phys. Lett. B* **178** (1986) 416.
- [2] F. Karsch, M. T. Mehr and H. Satz, *Color screening and deconfinement for bound states of heavy quarks*, *Z. Phys. C* **37** (1988) 617.
- [3] S. Digal, P. Petreczky and H. Satz, *String breaking and quarkonium dissociation at finite temperatures*, *Phys. Lett. B* **514** (2001) 57, arXiv: [hep-ph/0105234](https://arxiv.org/abs/hep-ph/0105234) [hep-ph].
- [4] N. Brambilla et al., *Heavy quarkonium: progress, puzzles, and opportunities.*, *Eur. Phys. J. C* **71** (2011) 1534, arXiv: [1010.5827](https://arxiv.org/abs/1010.5827).
- [5] A. Andronic et al., *Heavy-flavour and quarkonium production in the LHC era: from proton–proton to heavy-ion collisions.*, *Eur. Phys. J. C* **76** (2016) 107, arXiv: [1506.03981](https://arxiv.org/abs/1506.03981).
- [6] R. Rapp and X. Du, *Theoretical Perspective on Quarkonia from SPS via RHIC to LHC.*, *Nucl. Phys. A* **967** (2027) 216.
- [7] N. Krenz, H. van Hees and C. Greiner, *Quarkonia production in a Langevin approach.*, *J. Phys. Conf. Ser.* **1070** (2018) 012008, arXiv: [1805.10798](https://arxiv.org/abs/1805.10798).

- [8] X. Yao et al.,
Coupled Boltzmann transport equations of heavy quarks and quarkonia in quark-gluon plasma.,
JHEP **2021** (2021) 46, and private communication, arXiv: [2004.06746 \[hep-ph\]](https://arxiv.org/abs/2004.06746).
- [9] PHENIX Collaboration,
Measurement of $\Upsilon(1S + 2S + 3S)$ production in $p+p$ and $Au+Au$ collisions at $\sqrt{s_{NN}} = 200$ GeV.,
Phys. Rev. C **91** (2015) 024913, arXiv: [1404.2246](https://arxiv.org/abs/1404.2246).
- [10] STAR Collaboration,
Suppression of Υ production in $d+Au$ and $Au+Au$ collisions at $\sqrt{s_{NN}} = 200$ GeV.,
Phys. Lett. B **735** (2014) 127, arXiv: [1312.3675](https://arxiv.org/abs/1312.3675).
- [11] CMS Collaboration, *Measurement of nuclear modification factors of $\Upsilon(1S)$, $\Upsilon(2S)$, and $\Upsilon(3S)$ mesons in $PbPb$ collisions at $\sqrt{s_{NN}} = 5.02$ TeV*, *Phys. Lett. B* **790** (2019) 270,
arXiv: [1805.09215 \[hep-ex\]](https://arxiv.org/abs/1805.09215).
- [12] ALICE Collaboration,
Suppression of $\Upsilon(1S)$ at forward rapidity in $Pb-Pb$ collisions at $\sqrt{s_{NN}} = 2.76$ TeV,
Phys. Lett. B **738** (2014) 361, arXiv: [arXiv:1405.4493](https://arxiv.org/abs/1405.4493).
- [13] NA50 Collaboration, *ψ' production in $Pb-Pb$ collisions at 158 GeV/nucleon*,
Eur. Phys. J. C **49** (2007) 559, arXiv: [nucl-ex/0612013](https://arxiv.org/abs/nucl-ex/0612013).
- [14] NA50 Collaboration,
A new measurement of J/ψ suppression in $Pb-Pb$ collisions at 158 GeV per nucleon,
Eur. Phys. J. C **39** (2005) 335, arXiv: [hep-ex/0412036](https://arxiv.org/abs/hep-ex/0412036).
- [15] PHENIX Collaboration, *J/ψ production vs centrality, transverse momentum, and rapidity in $Au+Au$ collisions at $\sqrt{s_{NN}} = 200$ GeV*, *Phys. Rev. Lett.* **98** (2007) 232301.
- [16] STAR Collaboration,
Energy dependence of J/ψ production in $Au+Au$ collisions at $\sqrt{s_{NN}} = 39, 62.4$ and 200 GeV,
Phys. Lett. B **771** (2017) 13, arXiv: [arXiv:1607.07517](https://arxiv.org/abs/1607.07517).
- [17] ATLAS Collaboration, *Prompt and non-prompt J/ψ and $\psi(2S)$ suppression at high transverse momentum in 5.02 TeV $Pb+Pb$ collisions with the ATLAS experiment*, *Eur. Phys. J. C* **78** (2018) 762,
arXiv: [1805.04077 \[hep-ex\]](https://arxiv.org/abs/1805.04077).
- [18] CMS Collaboration, *Suppression and azimuthal anisotropy of prompt and nonprompt J/ψ production in $PbPb$ collisions at $\sqrt{s_{NN}} = 2.76$ TeV*, *Eur. Phys. J. C* **77** (2017) 252,
arXiv: [1610.00613 \[hep-ex\]](https://arxiv.org/abs/1610.00613).
- [19] ALICE Collaboration, *Differential studies of inclusive J/ψ and $\psi(2S)$ production at forward rapidity in $Pb-Pb$ collisions at $\sqrt{s_{NN}} = 2.76$ TeV*, *JHEP* **05** (2016) 179,
arXiv: [1506.08804 \[nucl-ex\]](https://arxiv.org/abs/1506.08804).
- [20] ATLAS Collaboration, *The ATLAS Experiment at the CERN Large Hadron Collider*,
JINST **3** (2008) S08003.
- [21] ATLAS Collaboration, *ATLAS Insertable B-Layer: Technical Design Report*,
ATLAS-TDR-19; CERN-LHCC-2010-013, 2010,
URL: <https://cds.cern.ch/record/1291633>, Addendum: ATLAS-TDR-19-ADD-1;
CERN-LHCC-2012-009, 2012, URL: <https://cds.cern.ch/record/1451888>.
- [22] B. Abbott et al., *Production and integration of the ATLAS Insertable B-Layer*,
JINST **13** (2018) T05008, arXiv: [1803.00844 \[physics.ins-det\]](https://arxiv.org/abs/1803.00844).

[23] ATLAS Collaboration, *Performance of the ATLAS trigger system in 2015*, *Eur. Phys. J. C* **77** (2017) 317, arXiv: [1611.09661 \[hep-ex\]](https://arxiv.org/abs/1611.09661).

[24] ATLAS Collaboration, *The ATLAS Collaboration Software and Firmware*, ATL-SOFT-PUB-2021-001, 2021, URL: <https://cds.cern.ch/record/2767187>.

[25] ATLAS Collaboration, *Muon reconstruction performance of the ATLAS detector in proton–proton collision data at $\sqrt{s} = 13$ TeV*, *Eur. Phys. J. C* **76** (2016) 292, arXiv: [1603.05598 \[hep-ex\]](https://arxiv.org/abs/1603.05598).

[26] J. Pumplin et al., *New Generation of Parton Distributions with Uncertainties from Global QCD Analysis*, *JHEP* **07** (2002) 012, arXiv: [hep-ph/0201195](https://arxiv.org/abs/hep-ph/0201195).

[27] T. Sjöstrand et al., *An introduction to PYTHIA 8.2*, *Comput. Phys. Commun.* **191** (2015) 159, arXiv: [1410.3012 \[hep-ph\]](https://arxiv.org/abs/1410.3012).

[28] G. T. Bodwin, E. Braaten and G. P. Lepage, *Rigorous QCD analysis of inclusive annihilation and production of heavy quarkonium*, *Phys. Rev. D* **51** (1995) 1125, arXiv: [hep-ph/9407339](https://arxiv.org/abs/hep-ph/9407339).

[29] ATLAS Collaboration, *The ATLAS Simulation Infrastructure*, *Eur. Phys. J. C* **70** (2010) 823, arXiv: [1005.4568 \[physics.ins-det\]](https://arxiv.org/abs/1005.4568).

[30] GEANT4 Collaboration, S. Agostinelli et al., *GEANT4 – a simulation toolkit*, *Nucl. Instrum. Meth. A* **506** (2003) 250.

[31] ATLAS Collaboration, *Measurement of the azimuthal anisotropy of charged particles produced in $\sqrt{s_{NN}} = 5.02$ TeV Pb+Pb collisions with the ATLAS detector*, *Eur. Phys. J. C* **78** (2018) 997, arXiv: [1808.03951 \[hep-ex\]](https://arxiv.org/abs/1808.03951).

[32] M. L. Miller, K. Reygers, S. J. Sanders and P. Steinberg, *Glauber Modeling in High-Energy Nuclear Collisions*, *Ann. Rev. Nucl. Part. Sci.* **57** (2007) 205, arXiv: [0701025 \[nucl-ex\]](https://arxiv.org/abs/0701025).

[33] ATLAS Collaboration, *Measurement of the $\Upsilon(1S)$ Production Cross-Section in pp Collisions at $\sqrt{s} = 7$ TeV in ATLAS*, *Phys. Lett. B* **705** (2011) 9, arXiv: [1106.5325 \[hep-ex\]](https://arxiv.org/abs/1106.5325).

[34] CMS Collaboration, *Measurement of the $\Upsilon(1S)$, $\Upsilon(2S)$ and $\Upsilon(3S)$ Polarizations in pp Collisions at $\sqrt{s} = 7$ TeV*, *Phys. Rev. Lett.* **110** (2013) 081802, arXiv: [1209.2922 \[hep-ex\]](https://arxiv.org/abs/1209.2922).

[35] CMS Collaboration, *Measurement of the prompt J/ψ and $\psi(2S)$ polarizations in pp collisions at $\sqrt{s} = 7$ TeV*, *Phys. Lett. B* **727** (2013) 381, arXiv: [1307.6070 \[hep-ex\]](https://arxiv.org/abs/1307.6070).

[36] LHCb Collaboration, *Measurement of J/ψ polarization in pp collisions at $\sqrt{s} = 7$ TeV*, *Eur. Phys. J. C* **73** (2013) 2631, arXiv: [1307.6379 \[hep-ex\]](https://arxiv.org/abs/1307.6379).

[37] M. Oreglia, *A Study of the Reactions $\psi' \rightarrow \gamma\gamma\psi$* , 1980, URL: <https://www.slac.stanford.edu/cgi-wrap/getdoc/slac-r-236.pdf>.

[38] Particle Data Group, *Review of Particle Physics*, *Prog. Theor. Exp. Phys.* **2020** (2020) 083C01.

[39] ATLAS Collaboration, *Measurement of quarkonium production in proton–lead and proton–proton collisions at 5.02 TeV with the ATLAS detector*, *Eur. Phys. J. C* **78** (2018) 171, arXiv: [1709.03089 \[hep-ex\]](https://arxiv.org/abs/1709.03089).

- [40] ATLAS Collaboration,
The simulation principle and performance of the ATLAS fast calorimeter simulation FastCaloSim,
 ATL-PHYS-PUB-2010-013, 2010, URL: <https://cds.cern.ch/record/1300517>.
- [41] ATLAS Collaboration,
Luminosity determination in pp collisions at $\sqrt{s} = 13$ TeV using the ATLAS detector at the LHC,
 ATLAS-CONF-2019-021, 2019, URL: <https://cds.cern.ch/record/2677054>.
- [42] N. Brambilla et al., *Bottomonium production in heavy-ion collisions using quantum trajectories: Differential observables and momentum anisotropy.*,
Phys. Rev. D **104** (2021) 094049, and private communication, arXiv: [2107.06222 \[hep-ph\]](https://arxiv.org/abs/2107.06222).
- [43] X. Du, M. He and R. Rapp,
Color Screening and Regeneration of Bottomonia in High-Energy Heavy-Ion Collisions.,
Phys. Rev. C **96** (2017) 054901, and private communication, arXiv: [1706.08670 \[hep-ph\]](https://arxiv.org/abs/1706.08670).
- [44] A. Mocsy, P. Petreczky and M. Strickland, *Quarkonia in the Quark Gluon Plasma.*,
Int. J. Mod. Phys. A **28** (2013) 1340012, arXiv: [1302.2180](https://arxiv.org/abs/1302.2180).
- [45] CMS Collaboration,
Suppression of excited Υ States Relative to the Ground State in $PbPb$ Collisions at $\sqrt{s_{NN}} = 5.02$ TeV,
Phys. Rev. Lett. **120** (2018) 142301, arXiv: [1706.05984 \[hep-ex\]](https://arxiv.org/abs/1706.05984).